

Large Eddy Simulation of turbomachinery flows using a high-order Implicit Residual Smoothing scheme

Jean-Christophe Hoarau*, Paola Cinnella* and Xavier Goerfelt*
Corresponding author: jean-christophe.hoarau@ensam.eu

* Arts et Métiers-ParisTech, DynFluid Laboratory, 151 bd. de l'Hôpital,
75013 Paris, France.

Abstract: A recently developed fourth-order accurate implicit residual smoothing scheme is investigated for the large eddy simulation of turbomachinery flows. Its accuracy, robustness and efficiency are assessed against test cases of increasing difficulty by means of comparisons with a high-accurate explicit Runge-Kutta scheme.

Keywords: LES, Implicit Residual Smoothing, Turbomachine

1 Introduction

Efficient direct numerical simulation and large eddy simulations (respectively DNS and LES) of compressible turbulent flows require a smart combination of numerical ingredients. Since computations must be carried out for extended periods of time in order to converge turbulent statistics, the choice of a suitable time integration scheme is of the utmost importance. Furthermore, highly stretched meshes are necessary to capture the fine-scale structures in turbulent boundary layers. With such small grid sizes, the stability constraint on time step of explicit time-marching methods becomes very restrictive in the near-wall regions. This constraint is much smaller than the time-step required to achieve a satisfactory accuracy level of the solution. A way of relaxing stability constraints consists in adopting an implicit time integration method. Unfortunately, this generally involves much larger computational and memory costs. As a consequence, fully implicit schemes are prohibitively expensive to use and some form of partial implicitation or approximate calculation of the Jacobians has to be used to reduce computational cost to an amenable level. The above indicates that the choice of a suitable implicit treatment for LES or DNS simulations derives from a delicate compromise between maximum allowable time step given, accuracy and stability constraints of the simulation and computational cost per iteration.

In the present work we evaluate the efficiency and accuracy of a recently developed high-order Implicit Residual Smoothing (IRS) method for the computation of complex unsteady flows, with focus on LES of turbomachinery flows. The IRS approach, initially proposed by Lerat and Sides [1] has been widely used in the past to speed up convergence of steady Euler and Navier-Stokes calculations based on Runge and Kutta time stepping. The present high-order IRS uses an implicit bi-Laplacian smoothing operator (of fourth-order accuracy) to filter out high-frequency modes of the residual, which leads to the solution of pentadiagonal systems for each space direction and Runge-Kutta stage. Thanks to the efficient inversion of scalar pentadiagonal matrices, the extra computational cost associated with the implicit operator remains much lower than standard implicit schemes.

The paper is organized as follows, section two presents the time and space integration schemes in this study. Section three reports numerical results for three well documented test cases allowing to preliminary assess the accuracy and the accuracy of the proposed IRS scheme. In section four IRS is applied to the LES of a severe high-pressure turbine cascade configuration. Finally section five contains some concluding remarks and future work perspectives.

2 Numerical methods

This study is focused on numerical methods for the solution of the compressible Euler and Navier-Stokes equations. The latter can be written in their instantaneous, Reynolds-averaged or filtered formulation supplemented by a turbulence or a sub-grid model. In the following of this section numerical methods are presented for a generic system of conservation laws of the form:

$$\frac{\partial w}{\partial t} + \nabla \cdot F(w) = S(w) \quad (1)$$

with $w \in \mathbb{R}^n$ the state vector of unknown variables of the problem, n being the number of scalar equations of the system, $F \in \mathbb{R}^{n \times d}$ the linear or non linear fluxes of the problem (d being the number of space dimensions) and $S \in \mathbb{R}^n$ the source terms, all depending on the chosen physical model. In a Cartesian reference frame, and if no source terms are present, equation (1) writes:

$$\frac{\partial w}{\partial t} + \sum_d \frac{\partial f_d(w)}{\partial x_d} = 0 \quad (2)$$

where the summation is carried out over the d space dimensions, f_d is the flux function in the d th direction, and x_d is the corresponding space coordinate. The flux functions contain an inviscid and a viscous part, denoted by superscripts e and v , respectively:

$$f_d = f_d^e - f_d^v.$$

After approximating the space derivatives by a suitable discretization scheme, equation (2) becomes:

$$w_t + \mathcal{R}(w) = 0 \quad (3)$$

where \mathcal{R} is the space approximation operator. The semi-discrete equation (3) represents a set of n ordinary differential equations, depending on the number of degrees of freedom, control volumes or grid points contained in each grid. In this work, space derivatives are approximated by means of structured finite-volume schemes. More precisely, the results reported in the following are based on a third-order and a ninth-order accurate approximation of the inviscid fluxes using five and eleven points per mesh direction, respectively. Such schemes are obtained by supplementing a fourth or tenth-order centered approximation, respectively, with a nonlinear artificial viscosity term using a blending of second and fourth (respectively tenth) derivatives [2, 3]. Such schemes are denoted DNC3 and DNC9 (for Directional Non Compact), respectively. All of the preceding numerical methods are implemented within the in-house structured finite-volume code DynHoLab [4].

2.1 Time integration schemes

In this section we first recall the baseline explicit time integration scheme, and then introduce the high-order implicit residual smoothing procedure.

2.1.1 Explicit Runge–Kutta scheme

The baseline explicit time integration scheme is the low-storage six-step optimized Runge–Kutta (RK6) method of Bogey and Bailly [5], largely used in the literature for LES and DNS calculation. This may be written in compact form as

$$\begin{cases} w^{(0)} & = & w^n \\ \Delta w^{(k)} & = & -a_k \Delta t \mathcal{R}(w^{(k-1)}), k = 1, \dots, s \\ w^{n+1} & = & w^{(s)} \end{cases} \quad (4)$$

where w^n is the numerical solution at time $n\Delta t$, $\Delta w^{(k)} = w^{(k)} - w^{(k-1)}$ is the solution increment at the k th Runge–Kutta stage, $s = 6$ is the number of stages, a_k are the scheme coefficients. The optimized coefficients

a_k can be found in [5]. The preceding RK6 is formally only second-order accurate but exhibits very low dispersion and dissipation errors up to the lowest resolved frequency for a given time-step Δt .

2.1.2 Implicit residual smoothing

The stability domain of the explicit RK schemes can be enlarged by using an implicit residual smoothing (IRS) technique. The main idea of IRS is to run the explicit scheme with a time step greater than the stability limit of the scheme. The scheme is then stabilized by smoothing the residual by means of a dissipative spatial operator added to the left hand side of equation (4). Most IRS operators introduced in the past were only first or second order accurate (e.g. [6, 7]), and introduced large additional dissipation and dispersion errors with respect to the baseline time scheme. In this work we extend the stability domain of the baseline RK6 by means of a recently proposed high-order IRS scheme [8]. The latter smooths the residuals by means of a bi-laplacian increment at each Runge-Kutta stage. In compact form this writes:

$$\begin{cases} w^{(0)} & = & w^n \\ \mathcal{J}\Delta w^{(k)} & = & -a_k\Delta t\mathcal{R}(w^{(k-1)}), k = 1, \dots, s \\ w^{n+1} & = & w^{(s)} \end{cases} \quad (5)$$

For a one-dimensional problem, the implicit operator \mathcal{J} is:

$$\mathcal{J} = 1 + \theta\left(\frac{\Delta t}{\delta x}\right)^4\delta(\lambda^e\delta^3) \quad (6)$$

where θ is a tuning parameter, λ^e the spectral radius of the inviscid flux jacobians and δ is the classical difference operator over one cell. An analytical study of the optimum value of θ for unconditional stability is difficult, but a numerical search shows that unconditional stability is obtained for [8]:

$$\theta \gtrsim 0.005$$

For multidimensional problems, the implicit operator is obtained by factorization of 1D operators in each mesh direction. Precisely, for a d -dimensional problem the IRS operator is of the form:

$$\mathcal{J} = \prod_{l=1}^d \left[1 - \theta\left(\frac{\Delta t}{\delta x_l}\right)^2\delta_l(\lambda_l^e\delta_l) \right] \quad (7)$$

where δx_l , δ_l and λ_l^e are, respectively, the space step, the difference operator and the spectral radius of the Jacobian flux in the l^{th} direction. The multidimensional IRS operator leads to the inversion of a pentadiagonal system per mesh direction at each Runge-Kutta stage. If required, the IRS operator can be applied only in space directions leading to a stiff behaviour (e.g. the direction normal to a solid wall), thus avoiding the inversion of systems in the other directions. For the governing Equation (2) the additional error introduced by the IRS operator with respect to the explicit scheme is of the form:

$$-\frac{1}{12}\theta\Delta t^4\sum_d(\lambda_d^e)^4\frac{\partial f_d^e}{\partial x_d^5} + O(\Delta t^4) \quad (8)$$

It is seen that the proposed IRS treatment introduces an additional error of $O(\Delta t^4)$, *ie.* higher than the baseline RK6. For this reason the scheme is referred-to as IRS4. Being proportional to a fifth derivative of the flux f_d^e , this error is recognized to have a dispersive nature. It becomes larger and larger as the smoothing coefficient is increased to stabilize the baseline scheme. A detailed study of the accuracy and stability of IRS4 can be found in [8].

2.1.3 Matrix systems for IRS schemes

The IRS4 applied at k^{th} Runge-Kutta step (5) leads to the inversion of a pentadiagonal matrix, presented hereafter in the simple case of a constant coefficient equation ($f_d = A_d w_d$ with A_d a constant matrix). When Dirichlet boundary conditions are applied, the solution increment at the boundary is set to 0. In this case,

the IRS operator leads to the inversion of the following $n \times n$ matrix:

$$\mathbf{J}_{n \times n} = \begin{pmatrix} \gamma & \alpha & \beta & 0 & 0 & 0 & 0 & 0 & \cdots & 0 \\ \alpha & \gamma & \alpha & \beta & 0 & 0 & 0 & 0 & \cdots & 0 \\ \beta & \alpha & \gamma & \alpha & \beta & 0 & 0 & 0 & \cdots & 0 \\ 0 & \beta & \alpha & \gamma & \alpha & \beta & 0 & 0 & \cdots & \vdots \\ \vdots & \ddots & \vdots \\ 0 & \cdots & 0 & \beta & \alpha & \gamma & \alpha & \beta & \cdots & 0 \\ \vdots & \ddots & \vdots \\ 0 & \cdots & 0 & 0 & 0 & \beta & \alpha & \gamma & \alpha & \beta \\ 0 & \cdots & 0 & 0 & 0 & 0 & \beta & \alpha & \gamma & \alpha \\ 0 & \cdots & 0 & 0 & 0 & 0 & 0 & \beta & \alpha & \gamma \end{pmatrix}$$

where $\beta = \theta CFL^4$, $\alpha = -4\beta$, $\gamma = 1 + 6\beta$, $CFL = \frac{\Delta t}{h} \lambda^e$ (with λ^e constant) and h the local mesh size.

For other kinds of boundary conditions (*ie.* Neumann, mixed or periodic) and at inter-subdomain boundaries (multi-block computations), two layers of ghost cells are used. This results in the inversion of a $(n+2) \times (n+2)$ matrix on each subdomain:

$$\mathbf{J}_{(n+2) \times (n+2)} = \begin{pmatrix} 1 & 0 & 0 & 0 & 0 & 0 & 0 & 0 & \cdots & 0 \\ 0 & 1 & 0 & 0 & 0 & 0 & 0 & 0 & \cdots & 0 \\ \beta & \alpha & \gamma & \alpha & \beta & 0 & 0 & 0 & \cdots & 0 \\ 0 & \beta & \alpha & \gamma & \alpha & \beta & 0 & 0 & \cdots & \vdots \\ \vdots & \ddots & \vdots \\ 0 & \cdots & 0 & \beta & \alpha & \gamma & \alpha & \beta & \cdots & 0 \\ \vdots & \ddots & \vdots \\ 0 & \cdots & 0 & 0 & 0 & \beta & \alpha & \gamma & \alpha & \beta \\ 0 & \cdots & 0 & 0 & 0 & 0 & 0 & 0 & 1 & 0 \\ 0 & \cdots & 0 & 0 & 0 & 0 & 0 & 0 & 0 & 1 \end{pmatrix}$$

Information in the layers of ghost cells is also used to compute the right-hand side of Eq. (5). For Neumann or mixed boundaries where $\frac{\partial(\Delta w^{(k)})}{\partial x_i}$ must be set to 0, the right-hand side term is extrapolated from the first inner cell :

$$\mathcal{R}(w^{(k-1)})_{1-j} = \mathcal{R}(w^{(k-1)})_1 \text{ for } j = \{1, 2\} \quad (9)$$

For inter-subdomain boundaries, ghost-cell information is transferred from the adjacent subdomain. This strategy is used for the parallel implementation of the method, leading to satisfactory results for a variety of LES simulations, like the ones presented in sections 3.2 and 4. Nevertheless it involves MPI exchanges between adjacent subdomains, which implies a communication overcost. The additional cost remains however rather small, so that the minimal cell number is about 50^3 in each block to keep a good scalability. The above-mentioned strategy may however deteriorate the overall stability at subdomain boundaries if very high CFL numbers are used. In the present simulations, based on maximal CFL numbers below 10 (limitation imposed by the proper resolution of the smallest time scales in DNS or LES), no stability problems were observed due to the boundary treatment. Finally, the efficiency and accuracy of the method at subdomain-boundaries could be further improved in the future, e.g. by using the approach described in [9]

3 Preliminary validations

In this section the accuracy and efficiency of IRS4 are first assessed for selected well-documented test cases of increasing complexity. These include the propagation of an acoustic pulse (gouverned by the Euler equations), the direct Navier-Stokes simulation of freely decaying homogeneous isotropic turbulence and a

preliminary application to the unsteady flow around a turbine cascade, solved at this stage by the unsteady RANS equations.

3.1 Propagation of an acoustic pulse

The IRS4 scheme is first assessed against the test case used in Kremer and al. [10]. In this case, the 2-D compressible Euler equations are used to model the flow. The mesh spacing in the x and y directions are named Δx and Δy respectively. A set of grids is considered whereby Δx is fixed, whereas $\Delta y \leq \Delta x$ is different for each mesh. The number of grid points in each mesh is $140 \times (140 \times \Delta x / \Delta y)$. For the spatial discretisation we consider both the third-order and the ninth-order accurate DNC schemes (see Section 2). The smoothing parameter of IRS4 is set equal to $\theta = 0.005$ and the dissipation parameters of DNC3 and DNC9 are $\{k_2 = 0.5 ; k_4 = 0.016\}$ and $\{k_2 = 0.5 ; k_{10} = 0.00015\}$ respectively. A simple extrapolation is applied at the domain boundaries and the initial conditions are defined by

$$p = p_0 + \Delta p \exp(-\ln(2) \frac{(x^2 + y^2)}{b^2}) \quad (10)$$

$$\rho = \rho_0 + (p - p_0)/c^2 \quad (11)$$

$$u_x = u_y = 0 \quad (12)$$

Where $b = 3\Delta x$, $p_0 = 10^5$ Pa, $\Delta p = 10$ Pa, $c = \sqrt{\gamma p_0 / \rho_0}$, $\rho_0 = p_0 / (T_0(\gamma - 1)c_v)$, $T_0 = 293K$ and $c_v = 717.5 J.K^{-1}.kg^{-1}$. Simulations are performed with RK6 and IRS4 schemes for aspect ratios $\Delta x / \Delta y = 1, 2, 4, 8, 16$ and 32 . The IRS4 is initially applied only in the y direction and then in both directions.

3.1.1 Stability limits

The aim here is to find the maximum initial CFL number ($CFL = c\Delta t / \Delta x$ with c the speed of sound of the medium at rest) ensuring stability. The maximum allowed CFL (CFL_{max}) is reported in Figure 1 as a function of the aspect ratio, for both schemes. The axes are in logarithmic scale. Results in Figure 1 are obtained by applying IRS4 only in the y direction. The IRS4 removes the dependency of the aspect ratio, although the maximum value is limited by the use of an explicit treatment in the x direction.

When applying IRS4 in both directions, $CFL_{max} \gg 10$ is found, independently of the spatial scheme order.

3.1.2 Accuracy

Afterwards, the accuracy of the IRS4 on anisotropic meshes is evaluated. The simulations are carried out up to $t = 32\Delta x / c$, and CFL numbers ranging between 0.1 and 2.0. The spatial scheme DNC9 is used in order to minimize the spatial discretization errors. The results are compared with a reference solution obtained using RK6 and a small CFL equal 0.01 for each mesh. The reference pressure field is displayed in Figure 2. The error rate E defined as :

$$E = \frac{\sqrt{\int \int_S (p - p_{ref})^2 ds}}{\sqrt{\int \int_S (p_{ref} - p_0)^2 ds}} \quad (13)$$

is evaluated for each mesh and reported on Figure 3 as a function of the CFL number for two different aspect ratio: uniform (panel a) and $\Delta x / \Delta y = 8$ (panel b). In the preceding equation p_{ref} is the reference pressure field at $CFL = 0.01$ and p the computed pressure. The error trend does not change significantly with the aspect ratio. Between $CFL = 0.1$ and $CFL = 0.8$ the IRS4 error is negligible and an overall convergence order similar to that of the RK6 scheme (second order accurate) is recovered.

Figure 4 displays the normalized error fields for the RK6 and IRS4 (applied in the y or in both directions). Using the IRS4 only in the y direction (Figure 4 b) leads to an anisotropic error distribution. On the other hand applying IRS4 in both directions (Figure 4 c) leads to a more isotropic repartition of the error (which is maximum in the directions aligned with the mesh) but to globally lower error levels than RK6.

The influence of the mesh aspect ratio on the error is illustrated in Figure 5 for the IRS4 in the y direction and

in Figure 6 for the IRS4 in both directions. The error anisotropy tends to increase slightly when increasing $\Delta x/\Delta y$. This effect is also visible when applying IRS4 in both direction.

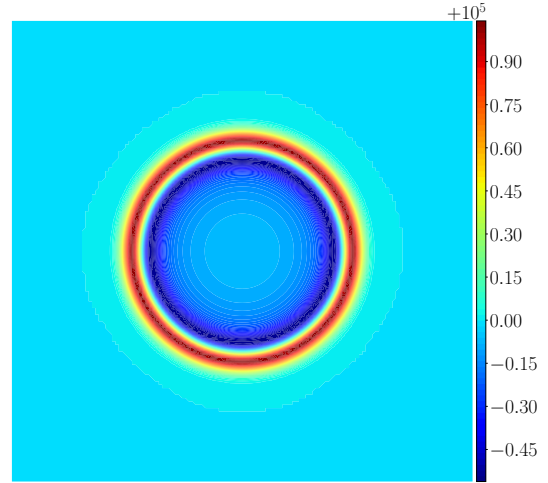
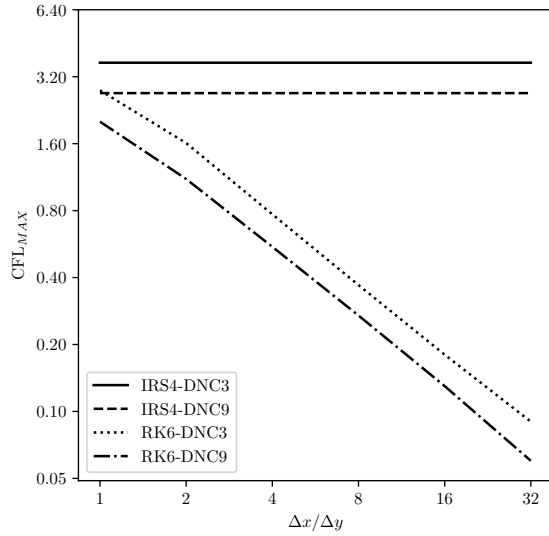
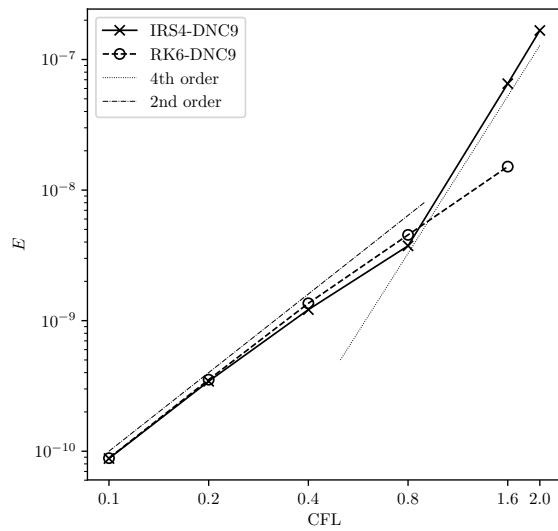
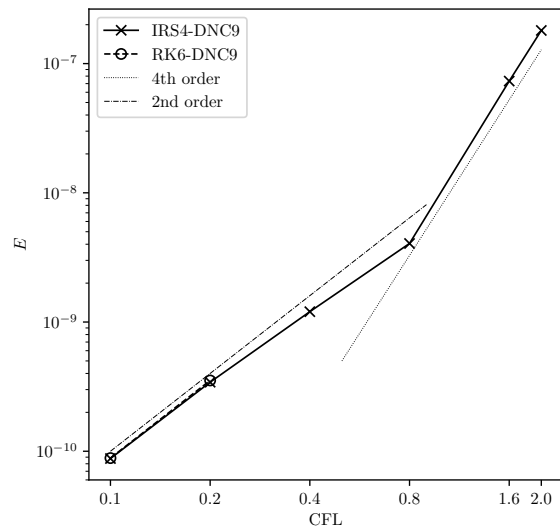


Figure 1: Maximum CFL number as a function of the aspect ratio $\Delta x/\Delta y$

Figure 2: Pressure field at CFL number of 0.01, $\Delta x/\Delta y = 1$ (scale in Pa), and at $t = 32\Delta x/c$

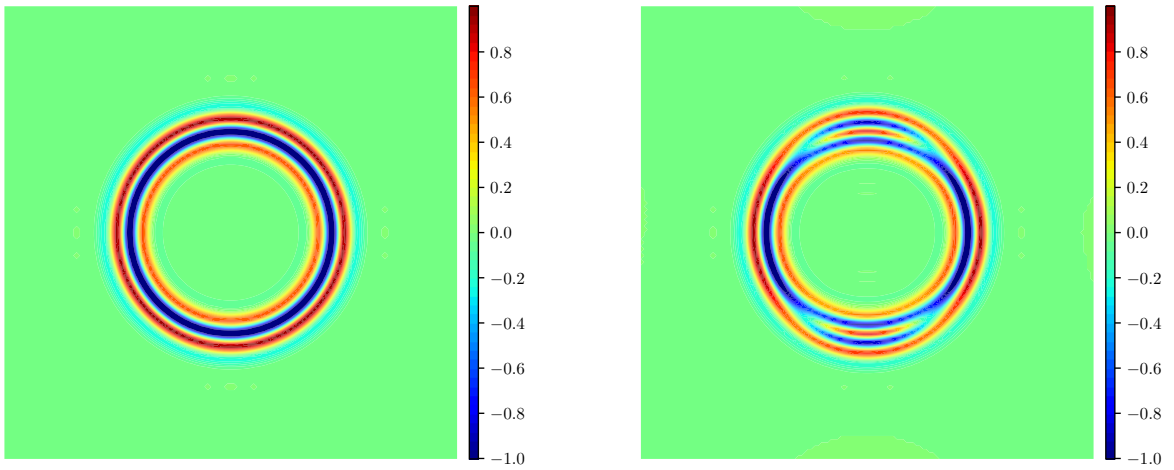


a)



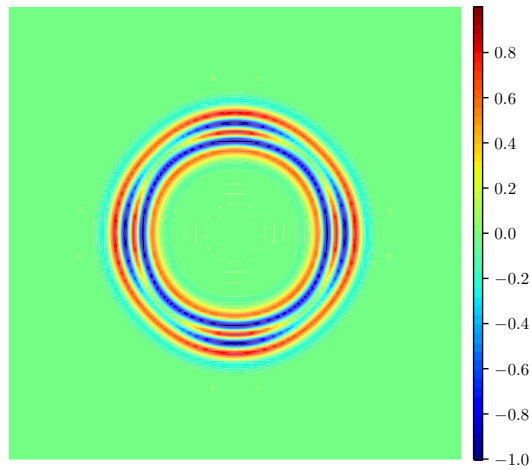
b)

Figure 3: Error rate as a function of the CFL number for: a) $\Delta x/\Delta y = 1$ and b) $\Delta x/\Delta y = 8$



a)

b)



c)

Figure 4: Distribution of normalized pressure error $(p - p_{ref}) / \max(p - p_{ref})$ at $CFL = 0.8$ and $\Delta x / \Delta y = 1$. a) RK6, b) IRS4 applied only in direction y and c) IRS4 applied in both directions.

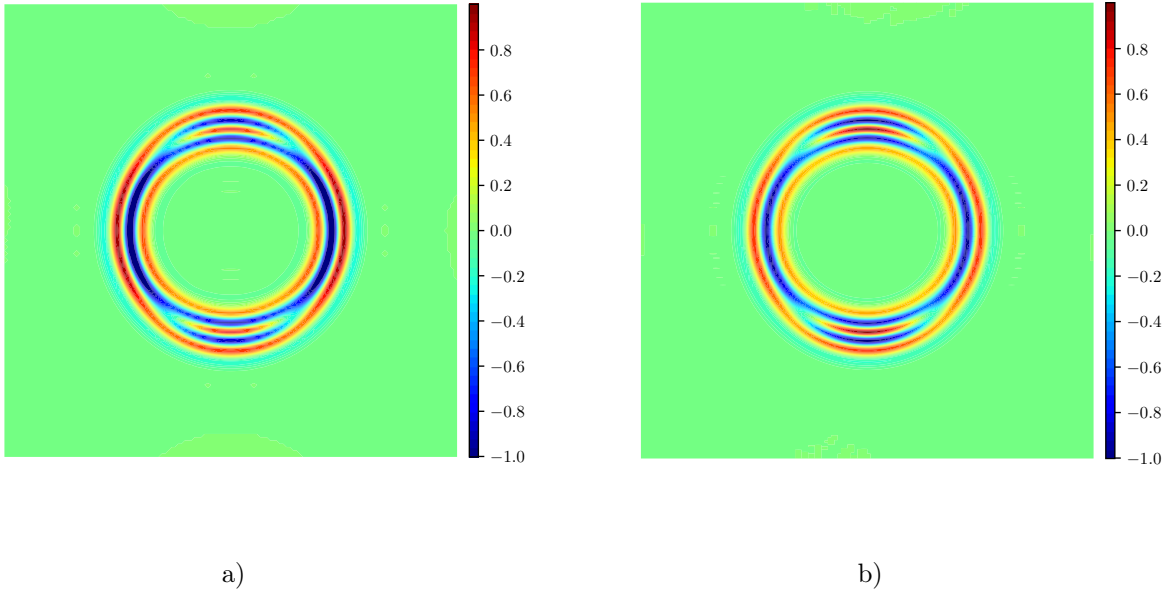


Figure 5: Distribution of the normalized pressure error $(p-p_{ref})/\max(p-p_{ref})$ at $CFL = 0.8$. IRS4 applied in y direction. a) $\Delta x/\Delta y = 1$ and b) $\Delta x/\Delta y = 32$

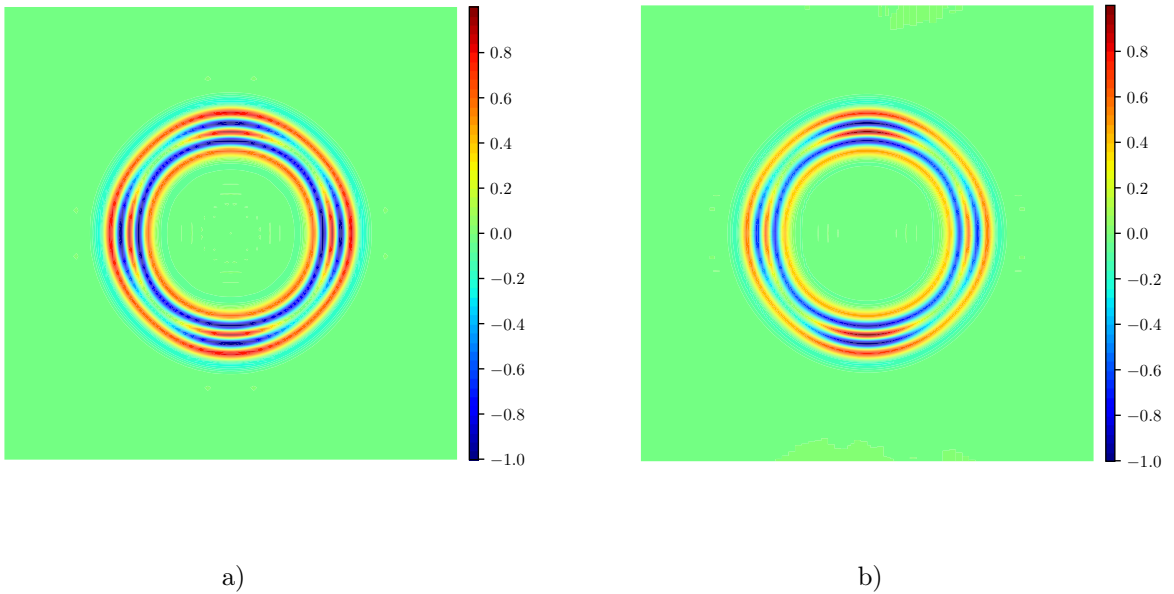


Figure 6: Distribution of the normalized pressure error $(p-p_{ref})/\max(p-p_{ref})$ at $CFL = 0.8$. IRS4 applied in both directions. a) $\Delta x/\Delta y = 1$ and b) $\Delta x/\Delta y = 32$

3.2 Homogeneous isotropic turbulence

In this section the IRS4 is applied to the DNS of a geometrically simple flow *ie.* the natural decay of homogeneous isotropic turbulence (HIT). The HIT decay is solved on a cubic computational domain with extension $[0, 2\pi]^3$. Periodic boundary conditions are imposed in the three Cartesian directions. The initial mean-square-root velocity is defined by prescribing the turbulent Mach number. Temperature and pressure fluctuations are specified in accordance with velocity fluctuations. The initial velocity spectrum is of the Passot and Pouquet [11] type:

$$E(k) = Ak^4 \exp \left[-2 \left(\frac{k}{k_0} \right)^2 \right] \quad (14)$$

where $k_0 = 4$ is the initial pic of energy and $A = 1$ the amplitude of the initial energy. The simulations were performed until a final time $t_f = 10\tau_{eddy}$ with τ_{eddy} the turnover time is define as:

$$\tau_{eddy} = \sqrt{\frac{32}{A}} (2\pi)^{1/4} k_0^{-7/2} \quad (15)$$

For the present simulations the ninth-order accurate DNC scheme is selected for space discretization (dissipation coefficient are imposed as $k_2 = 1.0$ and $k_{10} = 0.00028$). The computational domain is made of 128 points in each direction and the time step is defined as:

$$\Delta t = \frac{\Delta x}{(1 + 2M_{t_0})c_0} CFL_0 \quad (16)$$

where M_{t_0} the initial Mach number, CFL_0 the initial stability condition and c_0 the initial speed of sound. This is a less restrictive definition than the one used in [8] and leads to higher values of the time step for the same value of CFL_0 . Specifically, $CFL_0 = 10$ in [8] correspond $CFL_0 = 2.5$ with the present definition. Simulations were carried out at $M_{t_0} = 0.2$.

An overview of the flow is reported in Figure 7, which shows an isosurface of the Q-criterion colored by the velocity magnitude.

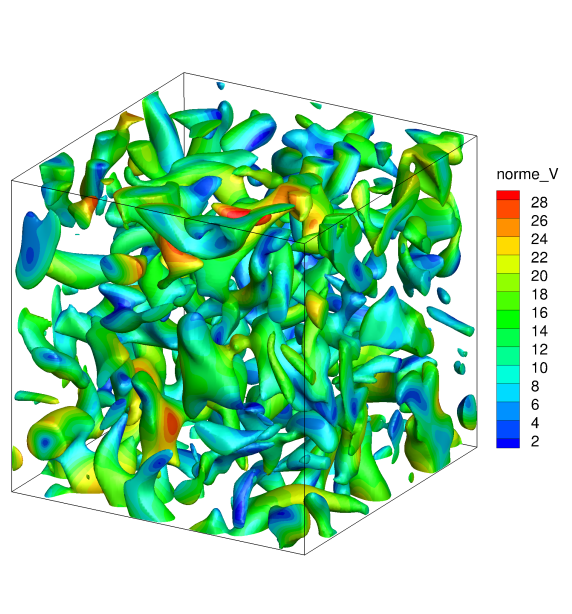


Figure 7: Iso-surface of the Q-criterion ($Q = 1000$) colored with the velocity magnitude at $t = t_f$ and IRS4 with $CFL = 5$

To evaluate the accuracy of the calculation the IRS4 is compared with a reference solution based on RK6 with a CFL number of 1. A set of simulations with IRS4 are carried out for CFL numbers equal to 5 and 10. Figure 8 displays the time evolution of the enstrophy Ω normalized by the initial enstrophy Ω_0 (panel a)), the skewness (panel b)) and the flatness (panel c)) of the velocity fluctuation gradient. The enstrophy Ω is defined as:

$$\Omega = \int_0^{\infty} k^2 E(k) dk \quad (17)$$

where k is the wave-number and $E(k)$ is the spectrum of the turbulent velocity integrated over shells of radius k . The skewness S_a and the flatness F_a of a random field a are defined as:

$$S_a = \frac{\langle a^3 \rangle}{\langle a^2 \rangle^{3/2}} \quad (18)$$

$$F_a = \frac{\langle a^4 \rangle}{\langle a^2 \rangle^{4/2}} \quad (19)$$

where the operator $\langle \bullet \rangle$ refer to a volume average over the computational domain at a fixed time instant. The IRS4 solution for Ω at $CFL_0 = 5$ is very close to the reference, while considerable differences are observed at $CFL_0 = 10$, leading to too large time step for correctly resolving the tiny structures populating the flow in the vicinity of the enstrophy peak. The high-order moments are more sensitive to the time discretization. Nevertheless, IRS4 with $CFL_0 = 5$ still ensures a rather satisfactory representation of the flow dynamics. Table 1 reports the overall computational time up to $t = t_f$ (CPU second on one Intel Xeon E5-2680V2 2.8GHz) as a function of the CFL number. One calculation iteration using IRS4 need approximately 1.5 times more CPU time than the same iteration using RK6. Despite the over-cost introduced by the inversion of the pentadiagonal systems, IRS4 leads to efficiency gains (for a similar solution accuracy) using $CFL_0 = 2 \div 5$. For higher values of CFL_0 numerical errors become too large.

CFL_0	1	1.25	2.5	5	10
RK6	36005.31	X	X	X	X
IRS4	X	45866.00	22932.14	11446.07	5999.42

Table 1: CPU time (second) as a function of the CFL and the time discretization

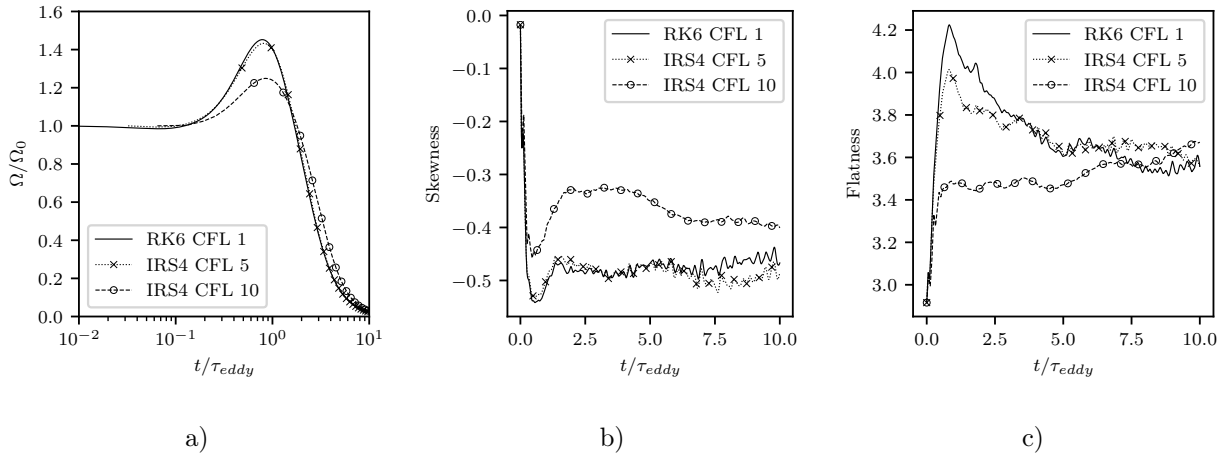


Figure 8: Comparison of the time evolution of a) normalized enstrophy b) skewness factor of the velocity fluctuation gradient and c) flatness factor of the velocity fluctuation gradient using IRS4 at various CFL numbers, comparison with reference solution using RK6 at $CFL_0 = 1$

3.3 Turbine cascade VKI LS-59

In view of LES of turbine flows IRS4 is preliminary applied to the unsteady flow around the VKI LS-59 transonic turbine rotor cascade previously considered in several experimental and numerical studies [12, 13, 14, 15]. The flow is modeled though the unsteady RANS equations, supplemented by the Wilcox $k - \omega$ [16] model of turbulence.

The configuration investigated experimentally in four European wind tunnel [17] is characterized by an outlet isentropic Mach number equal to 1. and by a Reynolds number (based on the chord and exit conditions) of 8.8×10^5 . The computational domain containing a single blade passage, is discretized by a C-grid of 384×32 grid points, with a first cell height leading to $\Delta y^+ \approx 2$. The third order DNC spatial scheme (using $k_2 = 0.5$ and $k_4 = 0.032$ as dissipation coefficients) is used for this series of calculations. Non reflective boundary conditions are applied at the inlet and outlet boundaries, and periodic conditions are applied at the lower and upper boundaries of the domain. The result of IRS4 (using $\theta = 0.02$ as smoothing parameter and $CFL \approx 5$) are compared to the available experimental data. Unsteady simulation are initialized with a (partially converged) steady RANS field.

In Figure 9 the computed iso-contours of the density gradient are compared to a Schlieren picture obtained experimentally by Kiock et al. [17] The flow is characterized by shock waves departing from the blade trailing edge and by vortex shedding in the wake. Figure 10 b) shows the time-averaged isentropic Mach number distribution along the blade. Present results are compared to experimental data from [17] and numerical results of [15], obtained using a Residual-Based-Compact scheme, IRS4 is in good agreement with the reference numerical data and matches reasonably well the experiments (which are highly uncertain). The largest differences observed are at the upper side in the vicinity of $x/c = 0.6$ (corresponding to the reflection of the impinging shock). Figure 10 a) shows the Fourier transform of the time-depending tangential force acting on the blade. A peak is observed for a Strouhal number (based on the leading edge thickness and exit velocity) of 0.21, corresponding to the shedding frequency. The latter is in excellent agreement with the previous numerical results [15] and in reasonable agreement with the range of frequency [0.2,0.4] observed experimentally for similar configuration [18]

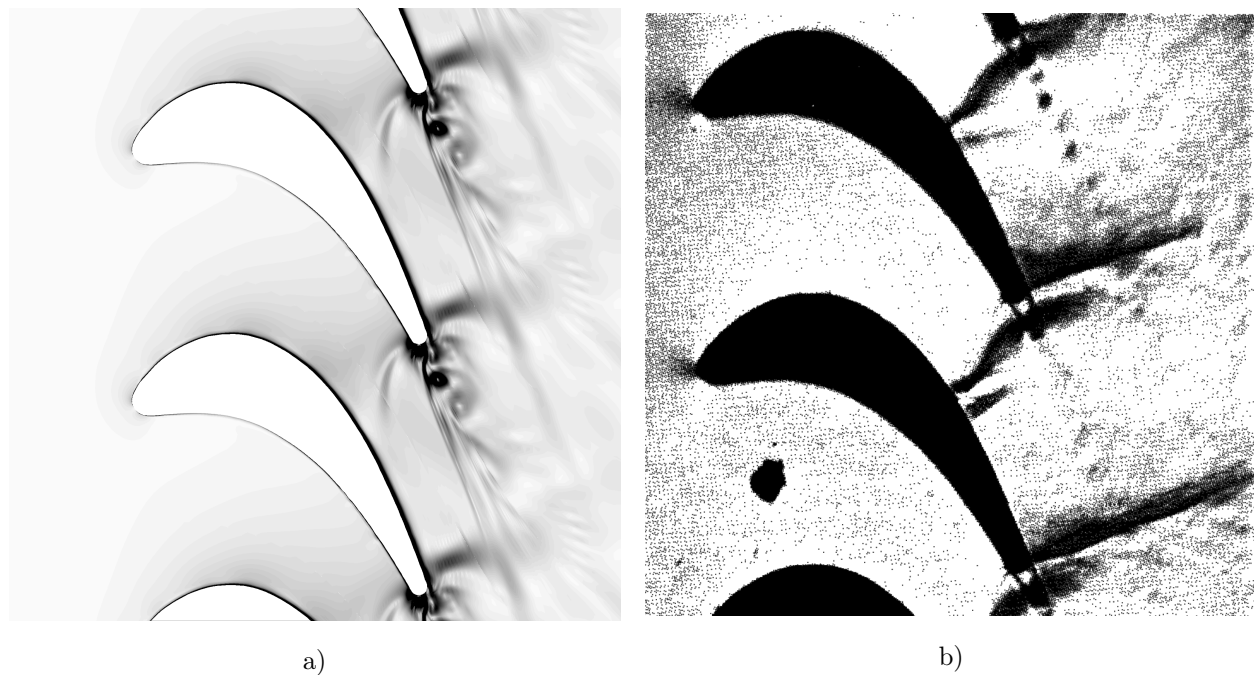


Figure 9: VKI LS-59 turbine cascade a) density gradient computed with IRS4 b) Schlieren picture experimented by Kiock and al. [17] ($M_{is} = 0.96$, $Re = 8.8 \times 10^5$)

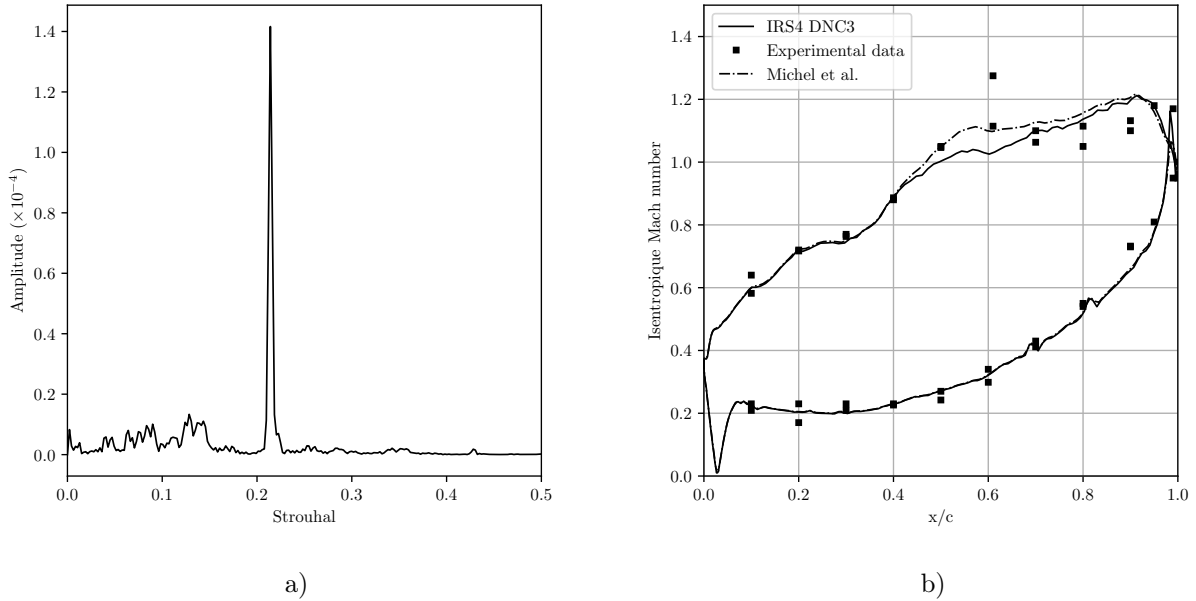


Figure 10: URANS of the VKI LS-59 cascade a) Fourier spectra of the tangential force applied on the blade and b) comparison of the time averaged wall distribution of the isentropic Mach number

4 Large-eddy simulation of the VKI LS-89 turbine cascade

In the present section, the IRS4 scheme is applied to the LES of the flow around a turbine cascade instrumented at the Von Karman Institute in 1990 by Arts et al. [19]. This configuration was chosen because experimental data are available, and because it has often been used as a test case for LES. Literature about this configuration is huge because experimental data are available for several flow conditions using the same set up. In the following of the section, we first describe the experimental setup and then we present the IRS4 results. These are compared with those generated by Collado et al. [20].

Arts and al. [19] carried out an experimental campaign to produce data for qualification of LES simulations. The tested configuration is a 2D turbine blade cascade, called the VKI LS-89 blade, described in [19]. The blade chord C is 67.647 mm long with a pitch-to-chord ratio of 0.85 a stagger angle of 55° . The flow angle at turbine inlet is equal to 0° . The flow condition simulated in the following correspond to experiment conditions named MUR129. These are characterized by outlet Reynolds number $Re_2 = 10^6$, and inlet free-stream turbulence intensity $Tu_0 = 1\%$. The total pressure at inlet is $P_0 = 1.87 \times 10^5 Pa$ and the static mean wall temperature is $T_w = 298K$. The isentropic Mach number at the outlet is $M_{is,2} = 0.840$.

A schematic view of the computation domain used for the present LES is displayed in Figure 11 a). The mesh is a H type structured mesh composed of 850 grid points in the stream-wise direction, 180 grid points in the pitch-wise direction and 200 grid points in the span-wise direction. The total number of grid points for the blade passage is equal to 30.6×10^6 . The blade is discretized by 550 grid points at the upper surface and the same number at the lower surface. The corresponding distribution of y^+ , x^+ and z^+ is displayed in Figure 11 b) c) and d). The average first layer size is $2.5\mu m$, leading to an average y^+ about 2. While the average x^+ is about 100 and the average z^+ is about 25. These values correspond to a coarse LES, but are similar to those of reference [20]. The present calculations are based on the DNC3 (using $k_2 = 0$ and $k_4 = 0.064$ as dissipation coefficients) scheme and IRS4 (using $\theta = 0.01$ as smoothing parameter). The LES is initialized with a preliminary 2D laminar calculation. A sinusoidal perturbation of the conservative variables with an amplitude of 10 % is applied for the span-wise direction to favor transition toward a fully 3D field. The dimensional time-step is set equal to 4×10^{-8} seconds, which correspond to a CFL number of approximately 10.

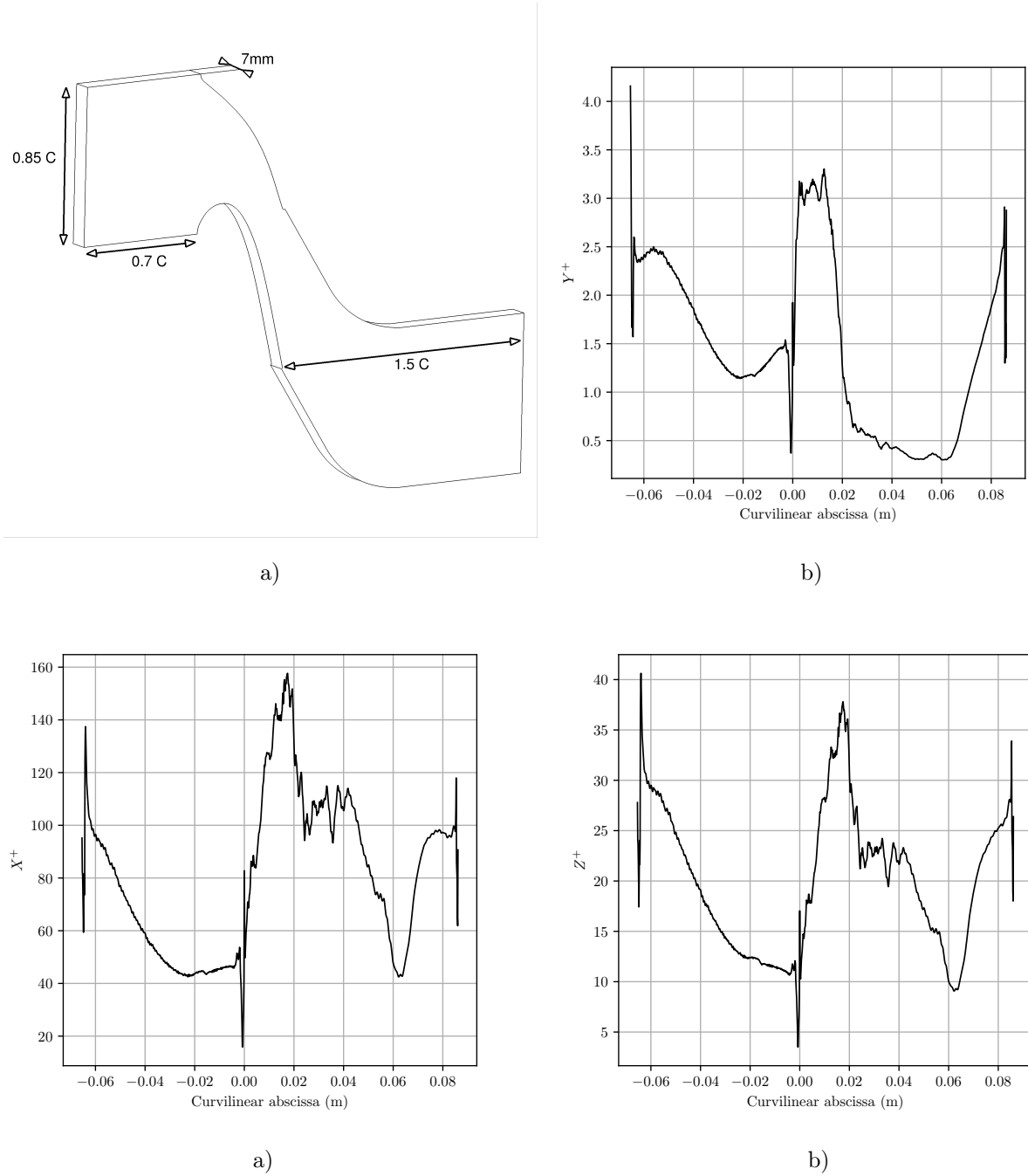


Figure 11: a) Mesh description where $C = 67.647\text{mm}$ and time-averaged wall distribution of b) y^+ c) x^+ and d) z^+ averaged in the span-wise direction.

In the following we present preliminary results, corresponding to zero inlet turbulent intensity. Calculations with $Tu \neq 0\%$ are planned as future work. The statistics are based on 2 flow-through time (time for a particle dropped at the inlet to reach the outlet $\approx 2\text{ms}$) taken after an initial transient of 3 flow-through times. The calculations are being continued and more converged results will be presented at the conference. Figure 12 displays the time averaged wall distribution of the isentropic Mach number and the convective heat transfer coefficient. The results are compared to the experimental data of [19] and to the numerical results of [20].

The isentropic Mach number does not match exactly the experiments, which correspond to case MUR43

(no Mach number data are available for MUR129). For MUR43 the inlet turbulence intensity and the outlet Mach and Reynolds number are the same as for MUR129, but the total inlet pressure is different $P_0 = 1.435 \times 10^5 Pa$. Present results match nicely with the calculation of reference [20].

Figure 12 b) presents the wall distribution of the convective heat transfer coefficient, defined as

$$H = \frac{q_w}{T_0 - T_w} \quad (20)$$

where q_w is the wall heat flux, T_0 the total free stream temperature and T_w the local wall temperature.

The present results are a bit noisy, due to the incomplete convergence of the flow statistics and to irregularities in the turbine blade geometry, leading to a non smooth wall normal along the blade. The present simulations are in rather good agreement with the experimental and numerical data from the literature. Specifically, the present LES provides a reasonably good prediction of the increase of H at the upper surface blade due to boundary layer transition. On the contrary the present simulation tends to under-estimate H along the first half of the upper surface and at near part of the lower surface. It is expected that the results could improve by using a non-zero turbulence intensity at the inlet. Finally an overview of the flow is shown in Figure 13 which report an iso-contour of the Q-criterion colored by the velocity magnitude.

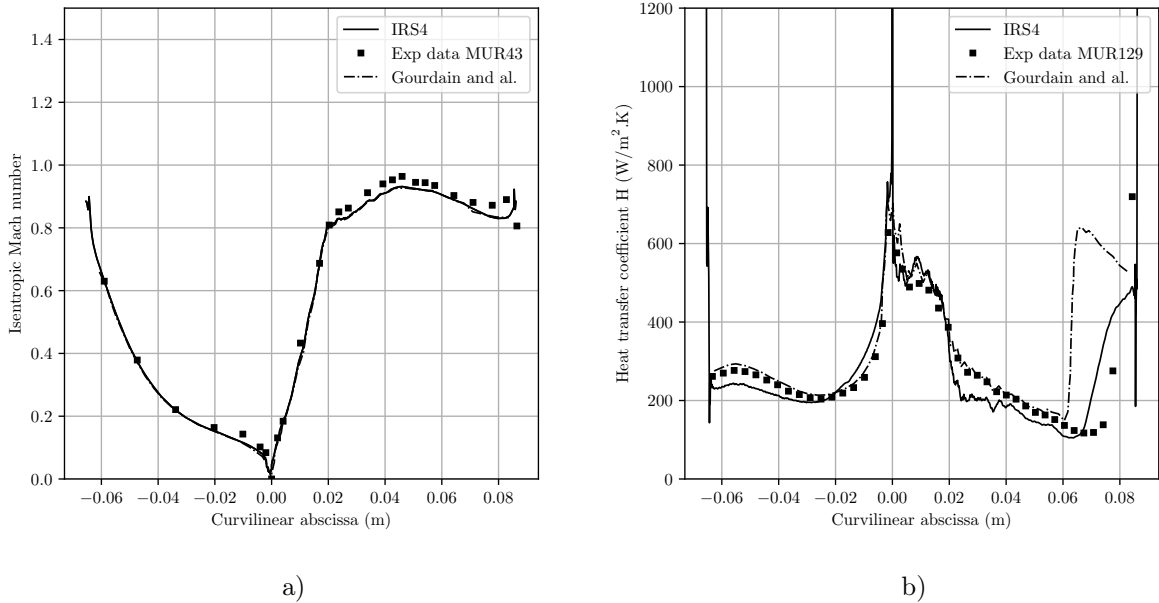


Figure 12: LES of the VKI LS-89 cascade comparison of Time-averaged wall distribution of a) the isentropic Mach number and b) the friction heat flux averaged in the span-wise direction.

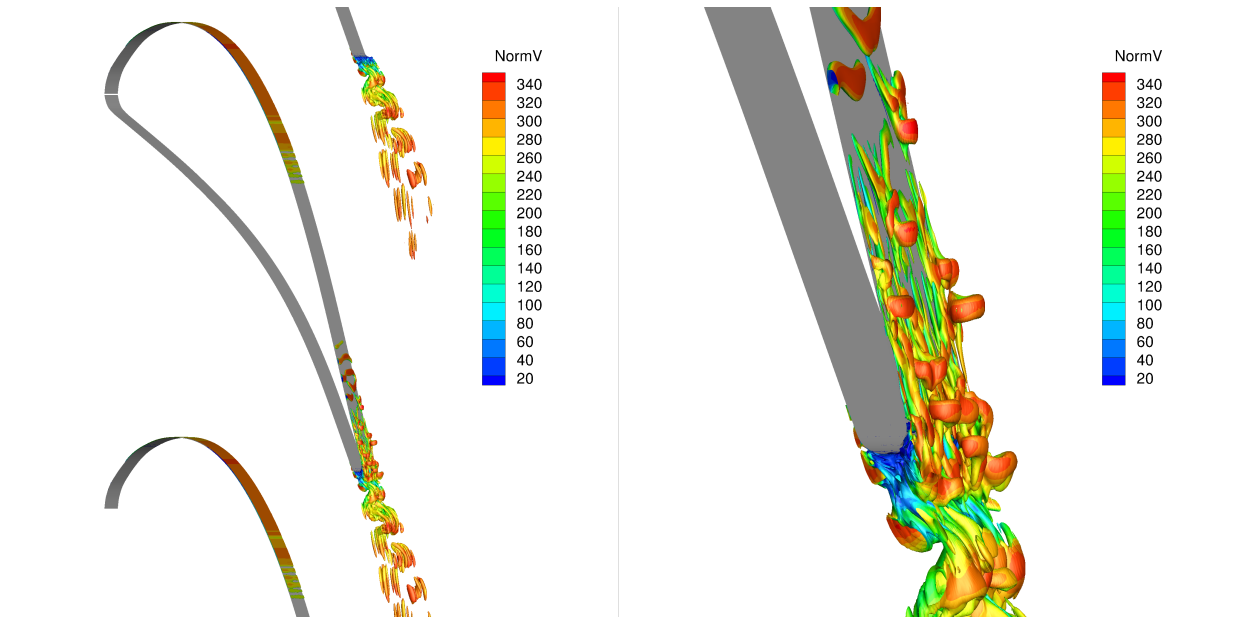


Figure 13: LES of the VKI LS-89 cascade iso-contour of the Q-criterion ($Q = 1 \times 10^{10}$) colorized with the norm velocity.

5 Conclusions

The IRS4 time integration scheme was investigated in this study. Accuracy and computational efficiency were compared with an optimized six step Runge and Kutta scheme. Three different test cases are considered namely, the acoustic pulse, homogeneous isotropic turbulence and two dimensional RANS simulation around turbine cascade VKI LS-59. The IRS4 based on the RK6 conserves the same theoretical order (second order accurate) removing the restrictive stability constraint on the maximum time step limitation. However to keep satisfactory accuracy, the CFL number must be kept below 10.

Afterwards, preliminary LES results for the LS-89 turbine cascade are presented. The simulations could be run with a CFL of approximately 10 at a moderate overcost. The results are found to be in rather good agreement with experimental data and numerical solutions from the literature. IRS4 thus appears to be a promising numerical technique to speed-up large eddy simulations of complex wall bounded flows while preserving solution accuracy.

Acknowledgments

This work was granted access to the HPC resources of IDRIS under the allocation A0032A07332 made by GENCI. Calculation were made on Ada composed of large memory SMP nodes (IBM x3750-M4) interconnected by a high-speed InfiniBand network. This study was also funded by the DGA (Direction Générale de l'Armement).

References

- [1] A Lerat, J Sidés, and Virginie Daru. An Implicit Finite-volume Method for Solving the Euler Equations. 170:343–349, 1982.
- [2] A. Jameson, W. Schmidt, and E. Turkel. Numerical solution of the euler equations by finite volume methods using Runge-Kutta time-stepping schemes. *AIAA Paper*, 1981.
- [3] J.W. Kim and D.J. Lee. Adaptive nonlinear artificial dissipation model for computational aeroacoustics. *AIAA Journal*, pages 810–818, 2001.

- [4] P.Y. Outtier, C. Content, P. Cinnella, and B. Michel. The high-order dynamic computational laboratory for CFD research and applications. *AIAA Paper*, 2013.
- [5] C. Bogey and C. Bailly. A family of low dispersive and low dissipative explicit schemes for flow and noise computations. *Journal of Computational Physics*, 194(1):194–214, 2004.
- [6] A. Jameson and T. Baker. Solution of the euler equations for complex configurations. *AIAA Paper*, 1983.
- [7] J. Blazek, N. Kroll, and C.-C. Rossow. A comparison of several implicit residual smoothing methods. *ICFD Conference on Numerical Methods for Fluid Dynamics*, 1992.
- [8] P. Cinnella and C. Content. High-order implicit residual smoothing time scheme for direct and large eddy simulations of compressible flows. *Journal of Computational Physics*, 326:1–29, 2016.
- [9] J. W. Kim. Quasi-disjoint pentadiagonal matrix systems for the parallelization of compact finite-difference schemes and filters. *Journal of Computational Physics*, 241:168–194, 2013.
- [10] F. Kremer, C. Bogey, and C. Bailly. Semi-implicit Runge-Kutta schemes: development and application to compressible channel flow. *AIAA Journal*, 52(3):516–527, 2014.
- [11] T. Passot and A. Pouquet. Numerical simulation of compressible homogeneous flows in the turbulent regime. *Journal of Fluid Mechanics*, 181:441–466, 1987.
- [12] D.T. Rubino, P. De Palma, G. Pascazio, and M. Napolitano. Solution of the steady euler equations using fluctuation splitting schemes on quadrilateral elements. *Computational Fluid Dynamics*, pages 101–106, 2009.
- [13] A. Arnone and R. Pacciani. Numerical investigation on wake shedding in a turbine rotor blade. *Fifteenth International Conference on Numerical Methods in Fluid Dynamics*, pages 358–363, 1997.
- [14] K. Grimich, B. Michel, P. Cinnella, and A. Lerat. Finite volume formulation of a third-order residual-based compact scheme for unsteady flow computations. *Lecture Notes in Computational Science and Engineering*, 99, 2014.
- [15] B. Michel, P. Cinnella, and A. Lerat. Multiblock residual-based compact schemes for the computation of complex turbomachinery flows. *International Journal of Engineering Systems Modelling and Simulation*, 27(1-2):2–15, 2011.
- [16] D.C. Wilcox. *Turbulence Modeling for CFD*. 1994.
- [17] R. Kiock, F. Lehthaus, N. Baines, and C. Sieverding. The transonic flow through a plane turbine cascade as measured in four european wind tunnels. *Journal of Engineering for Gas Turbines and Power*, 108(2):277–284, 1986.
- [18] H. Sieverding, Richard H., and Desse J.M. Turbine blade trailing edge flow characteristics at high subsonic outlet Mach number. *Journal of Turbomachinery*, 125(2):298–309, 2003.
- [19] T. Arts, M. Lambert de Rouvroit, and A.W. Rutherford. Aero-thermal investigation of a highly loaded transonic linear turbine guide vane cascade: A test case for inviscid and viscous flow computations. *NASA STI/Recon Technical Report*, 1990.
- [20] E. Collado Morata, N. Gourdain, F. Duchaine, and L. Gicquel. Effects of free-stream turbulence on high pressure turbine blade heat transfer predicted by structured and unstructured LES. *Int. J. of Heat and Mass Transfer*, 55(21):5754–5768, 2012.